PCCP

PAPER

View Article Online
View Journal | View Issue

Check for updates

Cite this: *Phys. Chem. Chem. Phys.*, 2025, **27**, 18651

Reaction mechanism of silylation of C–O bonds in alkyl ethers over supported gold catalysts: experimental and theoretical investigations

Yunosuke Tsunesada,[a] Tatsushi Ikeda,[a] Koki Muraoka,[a] Masafumi Doi,[b] Hiroki Miura,*[b] Tetsuya Shishido*[b] and Akira Nakayama*[a]

Received 25th May 2025,
Accepted 29th July 2025

DOI: 10.1039/d5cp01973g

rsc.li/pccp

The reaction mechanism of α-Fe_2O_3-supported Au-catalyzed silylation of ether $C(sp^3)$–O bonds by disilane is investigated using both experimental and computational approaches. The experimental study suggests that ether activation is the rate-determining step in the silylation of $C(sp^3)$–O bonds and that this reaction proceeds *via* an S_H2-type mechanism involving radical species. DFT calculations demonstrate that the Si–Si bond cleavage in disilane occurs at the interface between the Au cluster and the α-Fe_2O_3 support with a low activation energy and that the subsequent attack by silyl radicals on the ether involves an energy barrier, consistent with the experimental results. These investigations provide valuable insights into the unique reaction mechanism of ether $C(sp^3)$–O bond activation, which could serve as a basis for the development of novel supported metal catalyst systems for the utilization of ether compounds.

1. Introduction

Ether moieties are commonly found in natural compounds, and ethers are widely used as solvents, intermediates, and protective groups in organic synthesis due to their versatility and stability. Currently, the activation and direct functionalization of ether C–O bonds remain a significant challenge in organic and organometallic chemistry owing to their high bond dissociation energy and inherent chemical inertness,[1,2] which hinder the application of traditional methods for cleaving C–O bonds. Conventional approaches for the cleavage of the $C(sp^3)$–O bond in alkyl ethers typically require harsh conditions, such as heating with HBr, the use of strong Lewis acids,[3] or hydrogenolysis under high temperature and pressure conditions.[4–9] Therefore, the development of catalytic systems for direct functionalization of ether $C(sp^3)$–O bonds under mild conditions is of great importance for the efficient utilization of ethers.

Several transition-metal-based catalysts have been developed for the selective cleavage of $C(sp^3)$–O bonds in ethers. Organometallic complexes, such as Ir and Ni complexes, have been employed to activate these bonds, leading to efficient $C(sp^3)$–O bond functionalization. In particular, Ir catalysts have demonstrated considerable efficiency in the cleavage of $C(sp^3)$–O bonds in alkyl–alkyl ethers under mild conditions.[10] Also, Ni-catalyzed boron insertion into $C(sp^3)$–O bonds has also been reported.[11]

Organometallic complexes have thus proven to be effective for the activation of $C(sp^3)$–O bonds in alkyl ethers; however, the reusability of these homogeneous catalysts remains limited. On the other hand, supported metal catalysts have been widely employed in fine chemical synthesis, where the strong metal–support interaction provides unique reactivity and enhanced stability across various applications. For the selective cleavage of ether $C(sp^3)$–O bonds, Miura *et al.* reported the borylation of alkyl ethers using Au nanoparticles supported on α-Fe_2O_3, which exhibited high activity under mild conditions.[12] Silylation by disilanes through alky-silyl coupling to afford alkylsilanes represents another important reaction for selective cleavage of ether $C(sp^3)$–O bonds. Alkylsilanes serve as valuable scaffolds and intermediates in the synthesis of value-added molecules. Very recently, Miura *et al.* reported that Au nanoparticles supported on ZrO_2 efficiently promoted alkyl–silyl cross-coupling, enabling silylation of ethers with $C(sp^3)$–O bonds using disilanes to produce diverse alkylsilanes in high yields.[13] Notably, the reaction of branched cyclic alkyl ethers proceeded regioselectively, yielding products in which only the $C(sp^3)$–O bond with lower steric hindrance was cleaved (see Fig. 1 and also Fig. S1). These findings suggest that the reaction proceeds not through

---

[a] *Department of Chemical System Engineering, The University of Tokyo, Tokyo 113-8656, Japan. E-mail: nakayama@chemsys.t.u-tokyo.ac.jp*

[b] *Department of Applied Chemistry for Environment, Graduate School of Urban Environmental Sciences, Tokyo Metropolitan University, 1-1 Minami-Osawa, Hachioji, Tokyo 192-0397, Japan. E-mail: miura-hiroki@tmu.ac.jp, shishido-tetsuya@tmu.ac.jp*

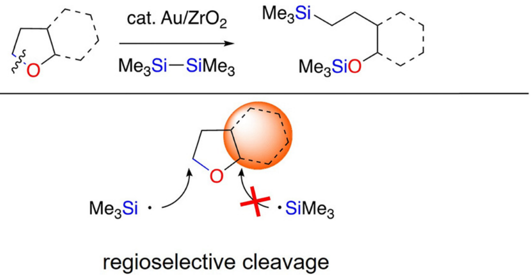

Fig. 1 Reaction scheme of Au/ZrO_2-catalyzed silylation of ethers with C(sp^3)–O bonds using disilanes to produce alkylsilanes.

carbocationic intermediates but rather *via* the S_H2 mechanism, characterized as a radical substitution reaction (see Fig. S2). It has been proposed that the cooperation of Au nanoparticles and metal oxide supports facilitates the generation of radical intermediates, thereby enabling efficient alkyl–silyl coupling.

These observations motivate us to investigate the reaction mechanism of supported Au-catalyzed silylation of ether C(sp^3)–O bonds using both experimental and computational approaches. Density functional theory (DFT) calculations are performed for the reaction between 2-methyltetrahydrofuran (2-MeTHF) and hexamethyldisilane (HMDS) as a model system. The use of a smaller cyclic ether allowed us to reduce the computational cost, while the inclusion of methyl substituents in 2-MeTHF is intended to discuss the regioselectivity of the reaction. We focus on the reaction mechanism catalyzed by Au nanoparticles supported on α-Fe_2O_3, as Au/α-Fe_2O_3 has exhibited superior catalytic activity compared to other supports in experimental studies. A detailed understanding of the structure of the active species and the underlying reaction mechanism is expected to provide valuable insights into the design and development of novel catalysts that facilitate the efficient utilization of ether compounds.

2. Experimental and computational details

2.1. Preparation of supported Au catalysts

The Au/α-Fe_2O_3 catalyst was prepared *via* a deposition–precipitation method using urea.[14] A total of 0.97 g of support material was added to 152 mL of an aqueous solution of $HAuCl_4$ (1 mM, the Au concentration in solution corresponds to a theoretical Au loading of 3 wt%) and urea (0.1 M). The suspension was heated at 80 °C and stirred vigorously for 16 h, during which the pH increased from approximately 3 to 8. The resulting dirty yellow precipitate was separated from the suspension and then washed three times with distilled water. The resulting powder was dried at 80 °C and subsequently calcined in air at 300 °C for 4 h to obtain supported Au catalysts. All other metal-oxide-supported Au catalysts, except Au/SiO_2, were prepared using the same deposition–precipitation method. The Au/SiO_2 catalyst was prepared *via* a deposition–precipitation method employing $Au(en)_2Cl_3$ as the Au precursor (see the SI for details).

2.2. DFT calculations

Spin-polarized DFT calculations were performed using pseudopotentials based on the projector-augmented wave (PAW) method. The VASP program package[15,16] was employed in this study. The Perdew–Burke–Ernzerhof (PBE) functional was used to describe the exchange–correlation potentials. A plane-wave cutoff energy of 600 eV was applied. The DFT+*U* method was utilized for the 3d orbitals of Fe atoms, and the value of the parameter was set to $U = 5.3$ eV, following the previous work.[17] To account for dispersion forces, the DFT-D3 method was used. Gaussian smearing with a smearing parameter of 0.05 eV was employed, and convergence criteria for the energy in the self-consistent field calculation and the force in the geometry optimization were set to 1×10^{-5} eV and 0.03 eV Å^{-1}, respectively. The transition state structures were located by the climbing-image nudged elastic band method (CI-NEB), followed by the dimer method to refine the obtained transition state structure. Frequency analysis confirmed that only one imaginary frequency exists in the transition state structures, except for negligible imaginary frequencies within numerical uncertainty.

α-Fe_2O_3 was considered as the support in this work, as it was experimentally determined to be the most effective support for this reaction (see the experimental results below). The lattice constants of bulk α-Fe_2O_3 were determined to be $a = b = 5.09$ Å and $c = 13.77$ Å through cell optimization using the 4 × 4 × 2 grid for *k*-point sampling, which was generated by the Monkhorst–Pack method. The calculated values were in good agreement with the experimental lattice parameters ($a = b = 5.03$ Å and $c = 13.74$ Å).[18] The most stable (110) surface with the O–Fe–O termination was considered in this work (see Table S1 for surface energy calculations).[19] The α-Fe_2O_3(110) surface contains five-coordinated Fe atoms and three- and four-coordinated O atoms. For modeling the α-Fe_2O_3(110) surface, a 5 × 1 supercell containing two O–Fe–O tri-layers was constructed, where the dimensions of the supercell were set to $a = 27.83$ Å, $b = 8.84$ Å, and $c = 24.54$ Å, with $\alpha = \beta = \gamma = 90$ degrees. A vacuum layer of 20 Å thickness was included to prevent interactions between periodic images. During the geometry optimization, the bottom O–Fe–O layer was fixed. The interface between Au and α-Fe_2O_3 was modeled using a rod model, where 24 Au atoms were placed on the α-Fe_2O_3(110) surface described above (see Fig. 2 for the slab model). The Au(111) surface was modeled as a periodic 4 × 4 supercell cleaved from its pre-optimized fcc structure, where the calculated lattice constant was determined to be $a = b = c = 4.07$ Å, which is consistent with the experimental value.[20] The Au slab model consists of four atomic layers, separated by approximately 15 Å of vacuum space along the *z*-direction. The dimensions of the Au(111) slab model were then set to $a = b = 11.52$ Å, $c = 26.16$ Å, $\alpha = \beta = 90$ degrees, and $\gamma = 120$ degrees. The Au–Au bond length in the top layer of the pristine Au(111) surface was 2.86 Å, and this value is consistent with the scanning tunneling microscopy (STM) measurement of 2.88 Å.[21] The two bottom layers were fixed during the geometry optimization. In all slab model calculations, the Brillouin zone was sampled only at the Γ point. For calculation of gas-phase molecules, only the Γ point was used, and a cubic simulation cell with $a = b = c = 20.0$ Å was employed.

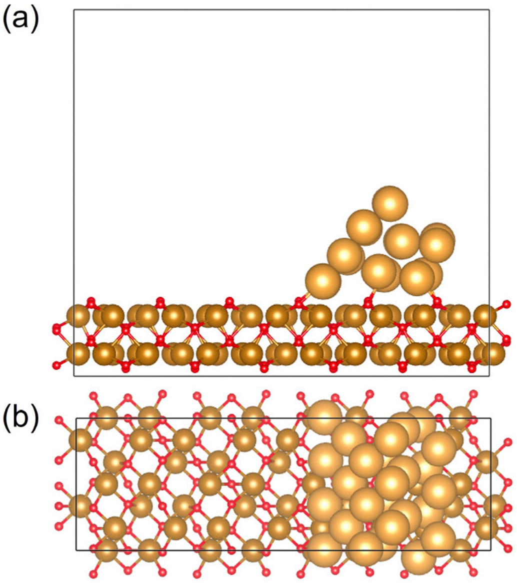

Fig. 2 (a) Side and (b) top view of the slab model of the Au/α-Fe_2O_3(110) interface. Color coding: brown for Fe, red for O, and light brown for Au.

The adsorption energy of a molecule E_A on the α-Fe_2O_3(110), Au(111), and Au/α-Fe_2O_3(110) surface is calculated according to

$$E_A = E_{\text{mol+surf}} - E_{\text{mol}} - E_{\text{surf}}$$

where $E_{\text{mol+surf}}$ is the total electronic energy of the surface–molecule system, while E_{surf} and E_{mol} are the energies of the surface without molecules and an isolated molecule, respectively. In this definition, the more negative value of adsorption energy indicates a stronger binding interaction with the surface.

3. Results and discussion

3.1. Optimization of catalysts and kinetic analysis

Previous experimental studies have shown that the coupling reaction between ether and HMDS occurs efficiently on the Au/ZrO_2 catalyst.[13] In this study, the initial examination focuses on evaluating the catalytic activity of metal oxide-supported Au catalysts for the reaction between decyl ether and HMDS. Among the five catalysts tested (Au/α-Fe_2O_3, Au/ZrO_2, Au/TiO_2, Au/Al_2O_3, and Au/SiO_2), the Au/α-Fe_2O_3 catalyst demonstrated the highest activity at 100 °C under an Ar atmosphere (see Table 1). Our previous study demonstrated that Au/α-Fe_2O_3 also exhibits high catalytic activity for the borylation of C(sp^3)–O bonds in allylic esters and alkyl ethers.[12] This was attributed to the high Lewis acid density and also strength of the Lewis acid sites on the metal oxide surface surrounding Au nanoparticles (see Table S3 and Fig. S11),[12,22] and thus it is suggested that the main catalytic active site for the silylation of C(sp^3)–O bonds in alkyl ethers is the interface between Au nanoparticles and the metal oxide support.

For the Au/α-Fe_2O_3 catalyst, the reaction orders with respect to decyl ether and HMDS were determined to be 1.1 and 0.4, respectively (Fig. 3). This result suggests that the rate-determining step is the activation of the ether. According to previous studies, the cleavage of the Si–Si bond in HMDS occurs on metal oxide-supported Au catalysts, leading to the formation of silyl cations and silyl radicals.[13,23] To further support a mechanism involving silyl radicals, radical-trapping experiments using 2,2,6,6-tetramethylpiperidine 1-oxyl radical (TEMPO) were carried out. The results confirmed that the progression of the alkyl–silyl coupling was inhibited, and silylated TEMPO was detected by gas chromatography-mass spectrometry (GC-MS) analysis (Fig. S3), suggesting the transient formation of silyl radicals. We believe that the generated silyl radicals are unlikely to diffuse freely into the gas phase, as the coupling reactions take place near the interface between Au nanoparticles and the α-Fe_2O_3 surface. Under these conditions, TEMPO likely acts as an effective inhibitor due to its strong interaction with the surface, which may facilitate the capture of radical species in close proximity to the surface.

3.2. Adsorption of 2-methyltetrahydrofuran and disilane on the Au/α-Fe_2O_3 surface

Using DFT calculations, the electronic properties of the Au/α-Fe_2O_3 model were first investigated. After the geometry optimization, Bader charge analysis revealed that Au atoms directly interacting with surface O atoms exhibit a positive charge

Table 1 Reaction of decyl ether and HMDS by metal oxide-supported Au catalysts

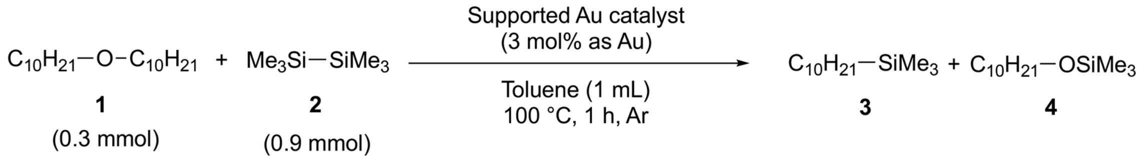

$$\underset{(0.3\ \text{mmol})}{\underset{\mathbf{1}}{C_{10}H_{21}{-}O{-}C_{10}H_{21}}} + \underset{(0.9\ \text{mmol})}{\underset{\mathbf{2}}{Me_3Si{-}SiMe_3}} \xrightarrow[\text{Toluene (1 mL)}\ 100\ {}^\circ\text{C, 1 h, Ar}]{\text{Supported Au catalyst (3 mol\% as Au)}} \underset{\mathbf{3}}{C_{10}H_{21}{-}SiMe_3} + \underset{\mathbf{4}}{C_{10}H_{21}{-}OSiMe_3}$$

Entry	Catalyst	Yield (%)
1	Au/α-Fe_2O_3	102[a]
2	Au/ZrO_2	90
3	Au/TiO_2	70
4	Au/Al_2O_3	5
5	Au/SiO_2	0

[a] Yields exceeding 100% are possible because the silyl ether product can undergo further reaction, leading to the formation of two alkylsilane molecules from a single ether molecule.

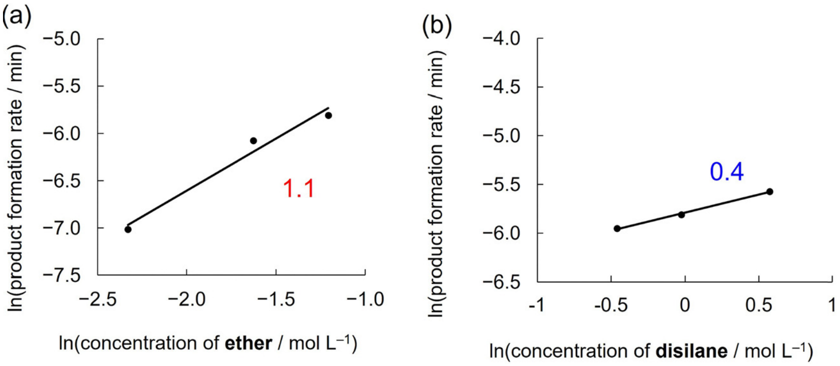

Fig. 3 Reaction order with respect to the concentration of (a) decyl ether and (b) HMDS.

ranging from +0.05*e* to +0.25*e* (Table S2). Overall, a net charge transfer of −1.1*e* from the Au rod model to the α-Fe_2O_3 surface was observed. This finding is consistent with X-ray photoelectron spectroscopy (XPS) measurements (Fig. S12), which indicate that Au atoms at the interface exhibit cationic properties.[12]

The adsorption structures of HMDS and 2-MeTHF were next investigated on the Au(111) and α-Fe_2O_3(110) surfaces, as well as at the interface between Au and α-Fe_2O_3, and the results are presented in Fig. 4 along with the adsorption energies. For HMDS, the strongest adsorption was observed at the interface between Au and α-Fe_2O_3, with an adsorption energy of −1.58 eV (Fig. 4(c)). In this configuration, one of the Si atoms is oriented towards the surface, while the other is located in close proximity to the Au atoms. The Si–Si bond length at the interface was calculated to be 2.38 Å, slightly longer than the gas-phase bond length of 2.36 Å. Bader charge analysis revealed a slight charge asymmetry between the two Si atoms, with the Si atom located near the Au atoms exhibiting a positive charge of +0.06*e* (Fig. S4). This observation is consistent with the charge distribution of the interface, where Au atoms interacting with the surface O atoms are more positively charged. Another adsorption structure at the interface (Fig. 4(d)) shows that the Si–Si bond is aligned parallel to the interface between Au and α-Fe_2O_3, and its adsorption energy is slightly weaker than that of the configuration shown in Fig. 4(c). In the case of 2-MeTHF, the molecule is also preferentially adsorbed at the interface, where the O atom of 2-MeTHF interacts with a surface Fe atom *via* acid–base interaction (Fig. 4(g)). The adsorption energy was calculated to be −3.17 eV, which is much stronger than that of HMDS at the interface (−1.58 eV). Adsorption of 2-MeTHF on the α-Fe_2O_3 surface is strong, with an adsorption energy of −2.36 eV (Fig. 4(f)), which is also stronger than that observed for HMDS.

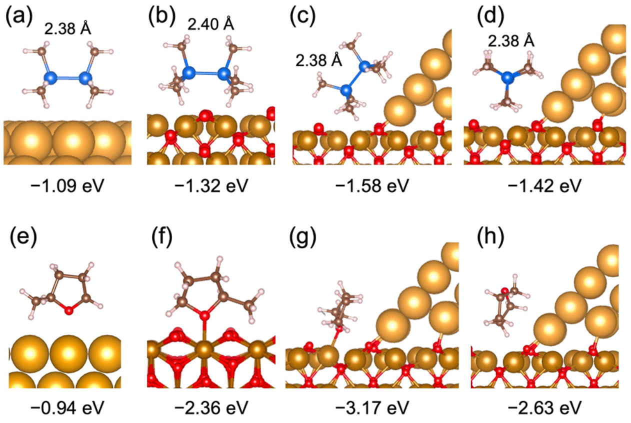

Fig. 4 Adsorption structures of HMDS and 2-MeTHF on (a) and (e) Au(111), (b) and (f) α-Fe_2O_3(110), and (c), (d), (g) and (h) at the Au/α-Fe_2O_3(110) interface. The Si–Si bond lengths of HMDS are also given. Color coding: brown for Fe, red for O, light brown for Au, blue for Si, white for H, and dark brown for C.

3.3. Energy profile for the Si–Si bond cleavage and silyl radical formation

Based on the results of adsorption structures described above, it is suggested that cleavage of the Si–Si bond occurs preferentially at the interface between the Au nanoparticle and metal oxide. Bader charge analysis and XPS measurements confirmed that cationic Au atoms are generated at the interface between Au nanoparticles and metal oxide support. Therefore, it has been proposed that a single-electron transfer from HMDS to the Au nanoparticles occurs, leading to the formation of a cationic radical species. Subsequently, cleavage of the Si–Si bond takes place, resulting in the generation of a silyl cation and a silyl radical.[13] Based on this proposed mechanism, we investigated the energy profile associated with the cleavage of the Si–Si bonds in HMDS at the Au/α-Fe_2O_3 interface.

Fig. 5 shows the potential energy profile for cleavage of the Si–Si bond at the Au/α-Fe_2O_3 interface. For comparison, cleavage on the α-Fe_2O_3 surface alone was also examined. The structures of the initial state (IS) were taken from the optimized adsorption structures for each system (Fig. 4(b) for the α-Fe_2O_3 surface and Fig. 4(c) for the Au/α-Fe_2O_3 interface). The energy barrier for Si–Si bond cleavage at the Au/α-Fe_2O_3 interface was determined to be 0.77 eV, whereas on the α-Fe_2O_3 surface, it was calculated to be 1.97 eV, indicating that the cleavage is energetically more favorable at the Au/α-Fe_2O_3 interface. Bader charges of the Si atoms at the initial state (IS), the transition state (TS), and the final state (FS) are shown in Fig. S5. On the α-Fe_2O_3 surface, the Bader charges of the Si atoms at the IS were close to zero. In contrast, at the Au/α-Fe_2O_3 interface, a charge bias between the two Si atoms (+0.06*e* and −0.08*e*) was

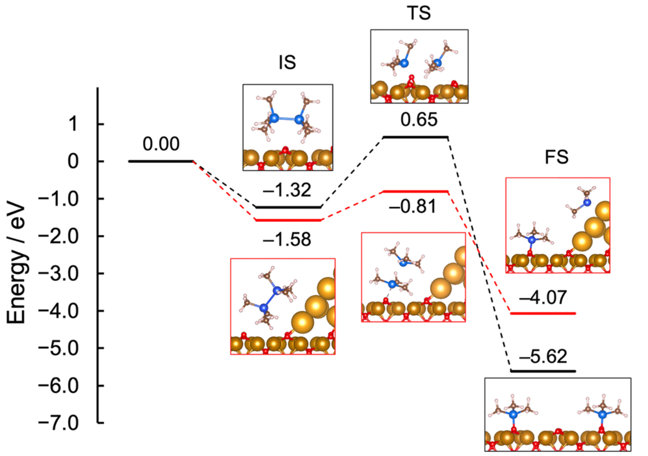

Fig. 5 Potential energy profile for the Si–Si bond cleavage on the α-Fe_2O_3 surface (black) and at the Au/α-Fe_2O_3 interface (red). Color coding: brown for Fe, red for O, light brown for Au, blue for Si, white for H, and dark brown for C.

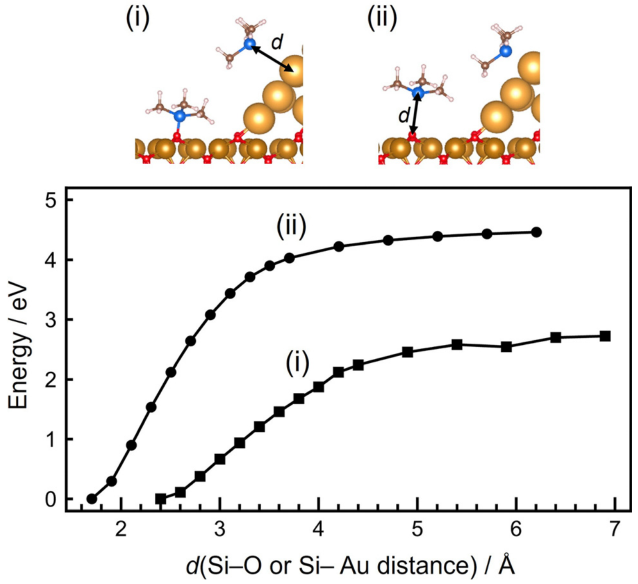

Fig. 6 Potential energy curves for the desorption process of each silyl radical, starting from the dissociative adsorption state. Color coding: brown for Fe, red for O, light brown for Au, blue for Si, white for H, and dark brown for C.

observed. In the dissociative adsorption at the FS, the Bader charge of the Si atom bound to the Au atoms increases to +0.80*e*, indicating that a single electron is transferred to the Au atoms.

From the dissociative adsorption state at the Au/α-Fe_2O_3 interface (shown as the FS in Fig. 5), the formation of radical active species was investigated. Fig. 6 shows the potential energy curves for the desorption process of each silyl radical, starting from the dissociative adsorption state. The potential energy curve was obtained by fixing the distance between each Si atom and its nearest (i) Au atom or (ii) O atom along the Si–Au or Si–O direction at the dissociative state, while optimizing all other degrees of freedom. The energies required for desorption of the silyl radical from the (i) Au atom or (ii) O atom were estimated to be 2.4 eV and 4.5 eV, respectively, indicating that desorption from the Au atom is energetically more favorable. The partial density of states (PDOS) of the Si(3p) orbitals during the desorption process is shown in Fig. S6. When the distance from the Au atom reaches 4.0 Å, formation of a radical species is confirmed from PDOS, where a clear asymmetry between the up-spin and down-spin is observed around the Fermi energy. We note that the desorption energy of 2.4 eV is relatively high considering the experimental conditions. Therefore, it is likely that silyl radicals do not desorb into the gas phase completely but instead remain in close proximity to the catalyst surface, as the reactions take place near the interface between Au nanoparticles and the α-Fe_2O_3 support. To further explore the behavior of silyl radicals on the surface, the activation energy for the migration of a silyl radical on the Au surface was calculated and found to be ∼0.3 eV (see Fig. S7). This low barrier suggests that surface migration of silyl radicals is energetically facile.

3.4. Ether C(sp^3)–O bond cleavage *via* the S_H2-type mechanism

After the formation of radical species, the next step involves cleavage of the ether C(sp^3)–O bond *via* attack by the silyl radical. Experimental results suggest that the reaction proceeds *via* a S_H2-type mechanism, characterized by a substitution reaction involving radical intermediates. As shown in Section 3.2, 2-MeTHF strongly adsorbs onto the α-Fe_2O_3 surface, with the O atom of 2-MeTHF interacting with a surface Fe atom (Fig. 4(f) and (g)). This adsorption structure facilitates selective radical attack at the α-carbon atom of the ether. Therefore, in this study, the attack of a silyl radical on the adsorbed 2-MeTHF species was considered. Fig. 7 shows the potential energy profile for the reaction between the silyl radical and adsorbed 2-MeTHF on α-Fe_2O_3 (shown in Fig. 4(f)). The activation energy for the C(sp^3)–O bond cleavage was calculated to be 1.18 eV, which is reasonable considering the experimental observations. This activation barrier is higher than that for the Si–Si bond cleavage of HMDS at the Au/α-Fe_2O_3 interface (0.77 eV), which is consistent with experimental results, indicating that the S_H2 reaction is the rate-determining step, and that the reaction order with respect to the ether is 1.1 (as described in Section 3.1). The overall potential energy profile for the reaction is presented in Fig. S9. The desorption energy of the alkyl silane product (1.74 eV) appears to be relatively high; however, it is important to note that additional factors, such as surface coverage and thermodynamics effects, particularly the contribution of translational entropy in the desorption process, need to be considered for a more quantitative comparison with experimental results.

We also examined the regioselectivity of the ether C(sp^3)–O bond activation. Attempts to calculate the activation barrier for cleavage of the other C(sp^3)–O bond on the α-Fe_2O_3 surface were unsuccessfully due to convergence issues in geometry optimization, as the targeted C(sp^3)–O bond was oriented away from the surface (see the IS in Fig. 7). To investigate the origin of this selectivity, gas-phase calculations were performed using

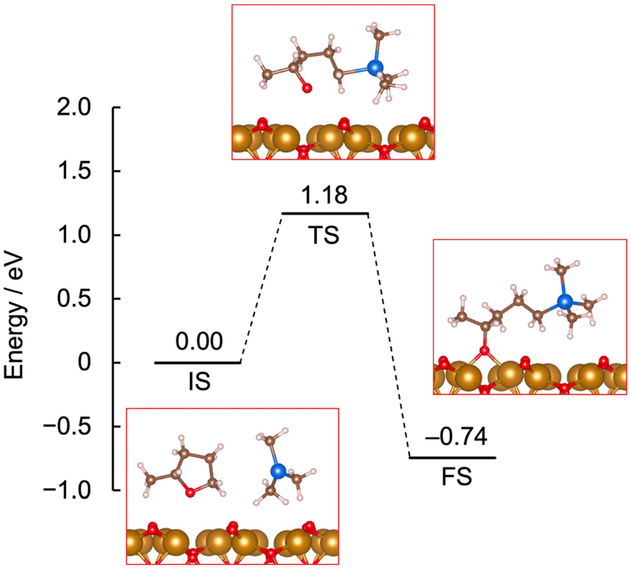

Fig. 7 Potential energy profile for cleavage of the ether C(sp^3)–O bond on the α-Fe_2O_3 surface. Color coding: brown for Fe, red for O, blue for Si, white for H, and dark brown for C.

the Gaussian software package, and it was clearly shown that cleavage of the less sterically hindered C(sp^3)–O bond is energetically more favorable, consistent with experimental observations and intuitive expectations (see Fig. S8). These results support the observed regioselectivity of the reaction.

4. Conclusions

The reaction mechanism of Au-catalyzed ether silylation was investigated using both DFT calculations and experimental approaches. The reaction between HMDS and 2-MeTHF was employed as a model system. Our findings indicate that the Si–Si bond readily dissociates at the interface between Au and α-Fe_2O_3 with a low activation energy of 0.77 eV. Subsequently, the silyl radical migrates from the Au atoms and attacks the 2-MeTHF molecule adsorbed onto the α-Fe_2O_3 surface. The C(sp^3)–O bond cleavage in the ether proceeds *via* the S_H2-type reaction, with the activation barrier for this step calculated to be 1.18 eV, which is reasonable considering the experimental observations. The continuous development of novel catalytic materials and a deeper understanding of the reaction mechanisms will contribute to the realization of more efficient and selective catalytic systems for the utilization of ether compounds.

Conflicts of interest

The authors declare no competing financial interest.

Data availability

Supplementary information available: scope of the branched cyclic ether, reaction mechanism of radical and ionic pathways, surface energy of the α-Fe_2O_3 slab model, results of radical-trapping experiments, Au–O bond length and Bader charge of the Au atoms at the Au/α-Fe_2O_3 interface, Bader charge of the Si atoms, PDOS along the potential energy curves for the desorption process of each silyl radical, potential energy profile for the migration of the silyl radical and cleavage of the ether C(sp^3)–O bond in the gas phase, overall potential energy profile, and details of experimental measurements (NMR spectra, HAADF-STEM images, NH_3-TPD profiles, X-ray photoelectron spectra, *etc.*). See DOI: **https://doi.org/10.1039/d5cp01973g**

Acknowledgements

The authors acknowledge the financial support from JSPS KAKENHI (grant numbers JP18H05247, JP24H00456, and JP24K01258), the JST FOREST Program (grant JPMJFR203V), and the MEXT Program: Data Creation and Utilization-Type Material Research and Development Project (Grant Number JPMXP1122712807) and JST SPRING (JPMJSP2108). Part of the calculations were performed on supercomputers at RCCS (Okazaki, project no. 25-IMS-C093), RIIT (Kyushu University), ACCMS (Kyoto University), and CCMS, IMR (Tohoku University, proposal no. 202412-SCKXX-0004).

References

1 D. F. McMillen and D. M. Golden, Hydrocarbon Bond Dissociation Energies, *Annu. Rev. Phys. Chem.*, 1982, **33**(1), 493–532, DOI: **10.1146/annurev.pc.33.100182.002425**.

2 Z. Qiu and C.-J. Li, Transformations of Less-Activated Phenols and Phenol Derivatives via C–O Cleavage, *Chem. Rev.*, 2020, **120**(18), 10454–10515, DOI: **10.1021/acs.chemrev.0c00088**.

3 B. C. Ranu and S. Bhar, Dealkylation of Ethers. A Review, *Org. Prep. Proced. Int.*, 1996, **28**(4), 371–409, DOI: **10.1080/00304949609356549**.

4 A. C. Atesin, N. A. Ray, P. C. Stair and T. J. Marks, Etheric C–O Bond Hydrogenolysis Using a Tandem Lanthanide Triflate/Supported Palladium Nanoparticle Catalyst System, *J. Am. Chem. Soc.*, 2012, **134**(36), 14682–14685, DOI: **10.1021/ja306309u**.

5 J. He, C. Zhao, D. Mei and J. A. Lercher, Mechanisms of Selective Cleavage of C–O Bonds in Di-Aryl Ethers in Aqueous Phase, *J. Catal.*, 2014, **309**, 280–290, DOI: **10.1016/j.jcat.2013.09.012**.

6 M. Wang, H. Shi, D. M. Camaioni and J. A. Lercher, Palladium-Catalyzed Hydrolytic Cleavage of Aromatic C–O Bonds, *Angew. Chem., Int. Ed.*, 2017, **56**(8), 2110–2114, DOI: **10.1002/anie.201611076**.

7 J.-P. Cao, T. Xie, X.-Y. Zhao, C. Zhu, W. Jiang, M. Zhao, Y.-P. Zhao and X.-Y. Wei, Selective Cleavage of Ether C-O Bond in Lignin-Derived Compounds over Ru System under Different H-Sources, *Fuel*, 2021, **284**, 119027, DOI: **10.1016/j.fuel.2020.119027**.

8 P. Kelley, S. Lin, G. Edouard, M. W. Day and T. Agapie, Nickel-Mediated Hydrogenolysis of C–O Bonds of Aryl Ethers: What Is the Source of the Hydrogen?, *J. Am. Chem. Soc.*, 2012, **134**(12), 5480–5483, DOI: **10.1021/ja300326t**.

9 M. Wang, Y. Zhao, D. Mei, R. M. Bullock, O. Y. Gutiérrez, D. M. Camaioni and J. A. Lercher, The Critical Role of Reductive Steps in the Nickel-Catalyzed Hydrogenolysis and Hydrolysis of Aryl Ether C–O Bonds, *Angew. Chem., Int. Ed.*, 2020, **59**(4), 1445–1449, DOI: **10.1002/anie.201909551**.

10 M. C. Haibach, N. Lease and A. S. Goldman, Catalytic Cleavage of Ether C–O Bonds by Pincer Iridium Complexes, *Angew. Chem., Int. Ed.*, 2014, **53**(38), 10160–10163, DOI: **10.1002/anie.201402576**.

11 H. Lyu, I. Kevlishvili, X. Yu, P. Liu and G. Dong, Boron Insertion into Alkyl Ether Bonds via Zinc/Nickel Tandem Catalysis, *Science*, 2021, **372**(6538), 175–182, DOI: **10.1126/science.abg5526**.

12 H. Nishio, H. Miura and T. Shishido, Low-Temperature Borylation of C(Sp^3)–O Bonds of Alkyl Ethers by Gold–Metal Oxide Cooperative Catalysis, *J. Am. Chem. Soc.*, 2024, **146**(50), 34690–34701, DOI: **10.1021/jacs.4c13003**.

13 H. Miura, M. Doi, Y. Yasui, Y. Masaki, H. Nishio and T. Shishido, Diverse Alkyl–Silyl Cross-Coupling via Homolysis of Unactivated C(Sp^3)–O Bonds with the Cooperation of Gold Nanoparticles and Amphoteric Zirconium Oxides, *J. Am. Chem. Soc.*, 2023, **145**(8), 4613–4625, DOI: **10.1021/jacs.2c12311**.

14 R. Zanella, S. Giorgio, C. R. Henry and C. Louis, Alternative Methods for the Preparation of Gold Nanoparticles Supported on TiO_2, *J. Phys. Chem. B*, 2002, **106**(31), 7634–7642, DOI: **10.1021/jp0144810**.

15 G. Kresse and J. Furthmüller, Efficient Iterative Schemes for *Ab Initio* Total-Energy Calculations Using a Plane-Wave Basis Set, *Phys. Rev. B:Condens. Matter Mater. Phys.*, 1996, **54**(16), 11169–11186, DOI: **10.1103/PhysRevB.54.11169**.

16 G. Kresse and J. Furthmüller, Efficiency of Ab-Initio Total Energy Calculations for Metals and Semiconductors Using a Plane-Wave Basis Set, *Comput. Mater. Sci.*, 1996, **6**(1), 15–50, DOI: **10.1016/0927-0256(96)00008-0**.

17 A. Kiejna and T. Pabisiak, Surface Properties of Clean and Au or Pd Covered Hematite (α-Fe_2O_3)(0001), *J. Phys.:Condens. Matter*, 2012, **24**(9), 095003, DOI: **10.1088/0953-8984/24/9/095003**.

18 L. W. Finger and R. M. Hazen, Crystal Structure and Isothermal Compression of Fe_2O_3, Cr_2O_3, and V_2O_3 to 50 Kbars, *J. Appl. Phys.*, 1980, **51**(10), 5362–5367, DOI: **10.1063/1.327451**.

19 R. Ovcharenko, E. Voloshina and J. Sauer, Water Adsorption and O-Defect Formation on Fe_2O_3(0001) Surfaces, *Phys. Chem. Chem. Phys.*, 2016, **18**(36), 25560–25568, DOI: **10.1039/C6CP05313K**.

20 E. R. Jette and F. Foote, Precision Determination of Lattice Constants, *J. Chem. Phys.*, 1935, **3**(10), 605–616, DOI: **10.1063/1.1749562**.

21 S. S. Batsanov, Size Effect in the Structure and Properties of Condensed Matter, *J. Struct. Chem.*, 2011, **52**(3), 602–615, DOI: **10.1134/S0022476611030231**.

22 H. Miura, K. Imoto, H. Nishio, A. Junkaew, Y. Tsunesada, Y. Fukuta, M. Ehara and T. Shishido, Optimization of Metal–Support Cooperation for Boosting the Performance of Supported Gold Catalysts for the Borylation of C–O and C–N Bonds, *J. Am. Chem. Soc.*, 2024, **146**(40), 27528–27541, DOI: **10.1021/jacs.4c08340**.

23 H. Miura, K. Ameyama and T. Shishido, Harnessing Supported Gold Nanoparticle as a Single-Electron Transfer Catalyst for Decarboxylative Cross-Coupling, *Adv. Synth. Catal.*, 2024, **366**(1), 62–69, DOI: **10.1002/adsc.202300462**.